Volume 11
Number 11
21 March 2023
Pages 3665–3892

Journal of Materials Chemistry C

Materials for optical, magnetic and electronic devices

rsc.li/materials-c

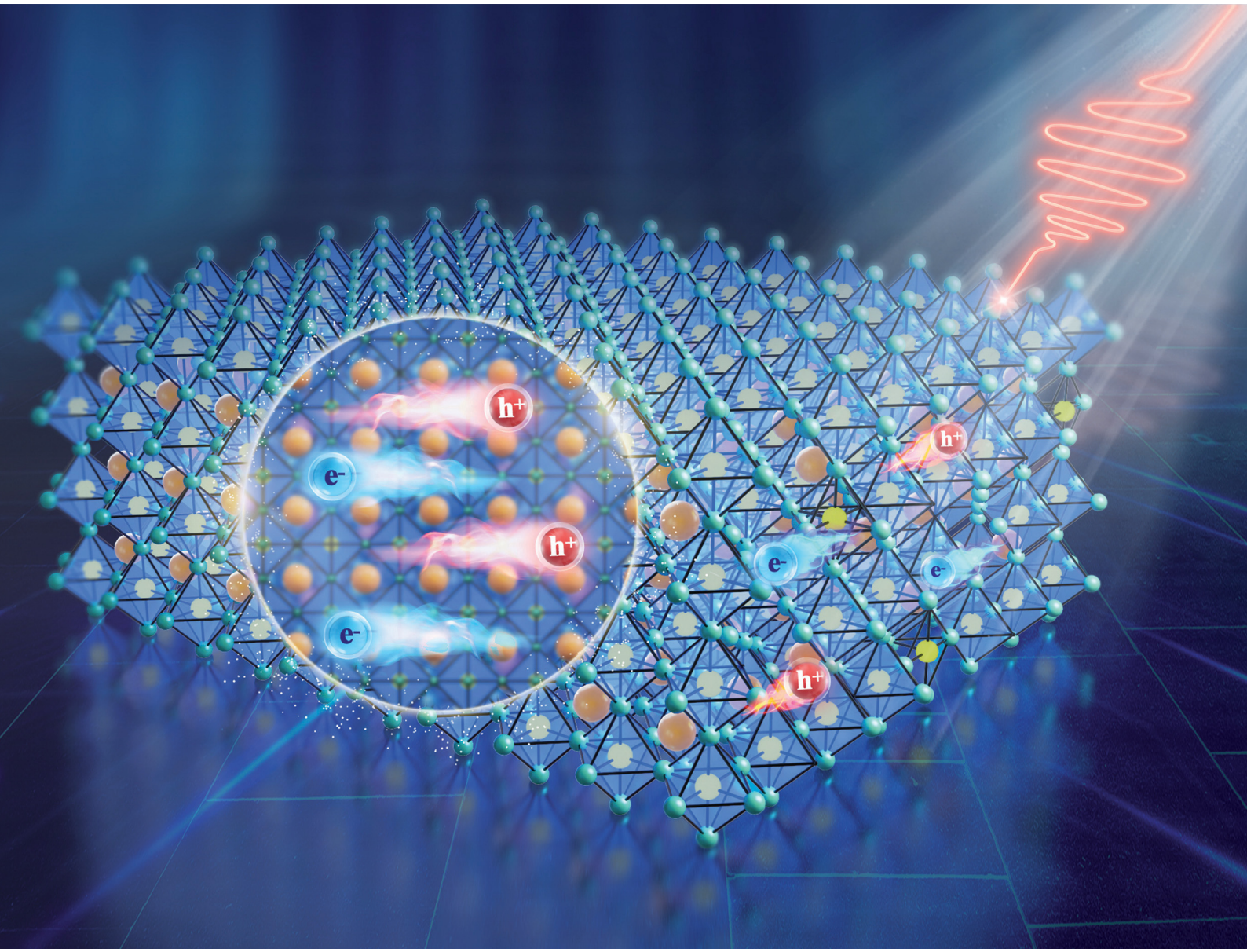

ISSN 2050-7526

ROYAL SOCIETY OF CHEMISTRY

PAPER
Lihe Yan *et al.*
Ultrafast photoinduced carrier dynamics in single crystalline perovskite films

10 YEARS ANNIVERSARY

Journal of Materials Chemistry C

ROYAL SOCIETY OF CHEMISTRY

PAPER

View Article Online
View Journal | View Issue

Check for updates

Cite this: J. Mater. Chem. C, 2023, 11, 3736

Ultrafast photoinduced carrier dynamics in single crystalline perovskite films†

Tianyu Huo, Lihe Yan, * Jinhai Si, Peipei Ma and Xun Hou

Received 29th August 2022,
Accepted 7th February 2023

DOI: 10.1039/d2tc03632k

rsc.li/materials-c

Photoinduced carrier dynamics of $CsPbBr_3$ single crystalline perovskite films were studied using femtosecond time-resolved transient absorption (TA) microscopy with a sub-micron spatial resolution. TA spectra of the internal area and boundary of perovskite films were obtained, respectively, and photoinduced carrier dynamic processes including hot carrier cooling, defect state trapping and carrier recombination were elucidated by singular value decomposition (SVD) and global fitting analysis of the TA spectra. Compared with the internal region, excited state absorption induced by the defects at the boundary was observed, and the shorter lifetimes of photoinduced carriers were attributed to the large number of defect states accelerating the non-radiative recombination of carriers. This work may provide further understanding about the influence of boundary defects on the performance of single crystalline perovskite devices.

Published on 09 February 2023. Downloaded by Xian Jiaotong University on 12/4/2023 7:34:49 AM.

1. Introduction

Perovskite, as an emerging semiconductor material,[1–3] has found many applications in photoelectric conversion devices, benefiting from its unique properties of a huge light absorption coefficient, tuneable band-gap, high carrier mobility, long diffusion distance, high defect tolerance, high photoelectric conversion efficiency and so on.[4–7] Compared with the commonly used polycrystalline perovskite films, a single crystal as a whole has exactly the same lattice structure, and suffers less from the effect of grain boundaries between crystalline grains and the high-density defects on the grain surface. Therefore, scattering and trapping are less likely to happen, and the photoinduced carriers can diffuse for a longer distance and have a longer lifetime.[8] For this reason, single crystalline materials are expected to be more suitable for fabricating photovoltaic and light emitting devices,[9–11] yet in fact, polycrystalline materials are used more widely in these devices with high conversion efficiencies.[12–14] One reason for single crystalline perovskite films being rarely used is that they are difficult to grow over a large area for the fabrication of devices.[15,16] On the other hand, the photovoltaic efficiency of single crystalline perovskites is not as high as expected, which could be due to the large concentration of defects on the surface and at the boundary of the single crystal.[17–21]

Previously, some works have been done to study the effects of defects in single crystalline perovskites on the photoinduced carrier behaviours and device efficiency. Bekir and co-workers proved by simulation that,[22] when the defect state concentration on the surface was reduced as much as possible, the device efficiency was easier to get close to the ideal state being free of defects. Zhu and co-workers found that when the thickness of single crystalline perovskite films decreased, the defect state concentration was increased and the fluorescence lifetime became shorter.[23] Using time-resolved photoemission electron microscopy (TR-PEEM), Liu *et al.* detected the photoelectron dynamics, and found that there were inhomogeneous and dense deep defect states on the surface of perovskites.[24] These research studies indicate that there is a high concentration of defect states on the surface and boundary of single crystalline perovskite films, which could have a serious impact on the performance of materials and devices.[25–27] Although, the methods mentioned above have been used to demonstrate the influence of defect states on carrier dynamics and device efficiency, the competition between the carrier dynamics introduced by defects and those that benefit optoelectronic conversion has not been demonstrated directly.

Femtosecond time-resolved transient absorption (fs-TA) spectroscopy has been demonstrated to be a powerful method to study the complex behaviours of photoinduced carriers taking place in semiconductors, including hot carrier cooling, defect state trapping, carrier recombination and so on.[28–30] In conventional fs-TA technology, the pump and probe beams are usually focused into the sample using a lens, and the spot size is about tens of microns. Therefore, the measured TA spectra are the ensemble averages of all samples in the whole irradiation

Key Laboratory for Physical Electronics and Devices of the Ministry of Education & Shaanxi Key Laboratory of Photonics Technology for Information, School of Electronic science and Engineering, Xi'an Jiaotong University, No. 28, Xianning West Road, Xi'an, 710049, China. E-mail: liheyan@mail.xjtu.edu.cn

† Electronic supplementary information (ESI) available. See DOI: https://doi.org/10.1039/d2tc03632k

This journal is © The Royal Society of Chemistry 2023

Published on 09 February 2023. Downloaded by Xian Jiaotong University on 12/4/2023 7:34:49 AM.

area, and the detailed information related to the inhomogeneity of the sample, such as elements and morphology nonuniformity, can't be extracted directly. To study the carrier dynamics of micro-scale samples, a fs-TA microscopy (fs-TAM) technique with high spatial resolution is developed, in which the pump and probe beams are focused to a sub-micron area using an objective lens.[31–33] From the fs-TAM measurements, photoinduced carrier dynamics in different regions of perovskite films might be distinguished, and their influence on the optoelectronic performance of the device could be unveiled.[34]

Here, we studied the photoinduced carrier dynamics of $CsPbBr_3$ single crystalline perovskite films, using a home-built fs-TAM system with a spatial resolution of about 650 nm. The 400 nm laser beam with a pump fluence of 24.11 μJ cm^{-2} and supercontinuum probe light were focused onto the internal and boundary of perovskite films, respectively, and the TA spectra at both regions were acquired. Through singular value decomposition (SVD) and global fitting analysis, photoinduced carrier dynamic processes including hot carrier cooling, defect state trapping and carrier recombination were elucidated. Compared with the internal region, photoinduced carriers at the boundary showed shorter lifetimes, which could be due to the large number of defect states accelerating the non-radiative recombination of carriers. Besides, an additional transient absorption induced by the dense defects at the boundary was observed. Findings of the study may help to understand the influence of defects in single crystalline perovskite materials on the photophysical properties of carriers, and provide guidance for optimizing device performance.

2. Results and discussion

Single crystalline perovskite ($CsPbBr_3$) films were prepared by the space-limited method as described in the literature.[35] The specific process is described in the Experimental Methods. First, the morphology and chemical properties of the film were characterized. Fig. 1(a) shows the scanning electron microscope (SEM) image of the sample. The sample shows a large size (tens of microns), as well as a smooth and clean surface, which could be due to slow crystallization assisted by the anti-solvent diffusion process. The internal and boundary regions tested in the experiment were marked with red dashed boxes. As displayed in the atomic force microscope (AFM) image in Fig. 1(b), the thickness of the film is estimated to be about 450 nm and the surface flatness is good. Fig. 1(c) shows the multi-element mapping images and the Energy Dispersive Spectroscopy (EDS) element analysis results. The element distribution is uniform and the calculated element content ratio of the sample is about Cs : Pb : Br ≈ 14 : 19 : 67, which is in accordance with the element ratio of the $CsPbBr_3$ perovskite. Fig. 1(d) shows the photoluminescence spectrum (PL) of the sample with the peak centred at 530 nm, being consistent with some previous results.[35]

To study the carrier dynamics of micro-scale samples, fs-TAM measurements with high spatial resolution were performed by focusing the pump and probe beams in the micro-region of the sample using an objective lens. Firstly, the internal region was studied and the experimental results are shown in Fig. 2. We conducted tests in six random locations at the internal region under the same experimental conditions, and these experimental results are displayed in Fig. S1 of the ESI.†

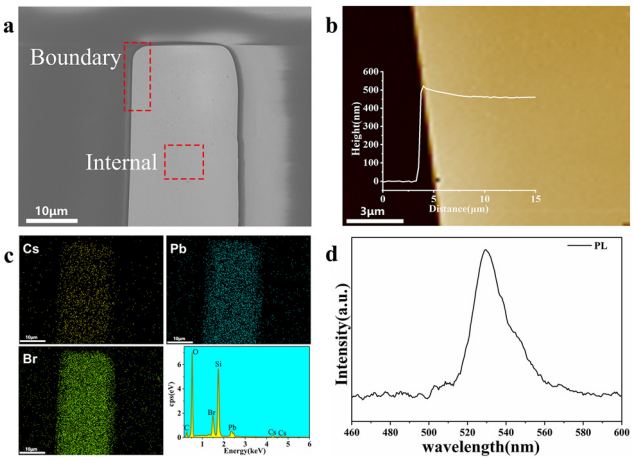

Fig. 1 (a) SEM image of a single crystalline $CsPbBr_3$ film, (b) AFM characterization results, (c) element mapping images, and EDS analysis and (d) the PL spectrum of a single crystalline $CsPbBr_3$ film.

Fig. 2(a) shows the pseudo colour diagram of the TA signal acquired at the internal region of the $CsPbBr_3$ film. We can easily find that there are three obvious signal bands in the figure, namely, the negative absorption signal with a central wavelength of 515 nm (PB1), the first positive absorption signal with a central wavelength of 530 nm (PA1) and the second positive absorption signal with a central wavelength of 495 nm (PA2). Among these signals, negative PB1 and positive PA2 signals exist for a long time, while positive PA1 exists only for a few picoseconds, as shown by the temporal evolution of

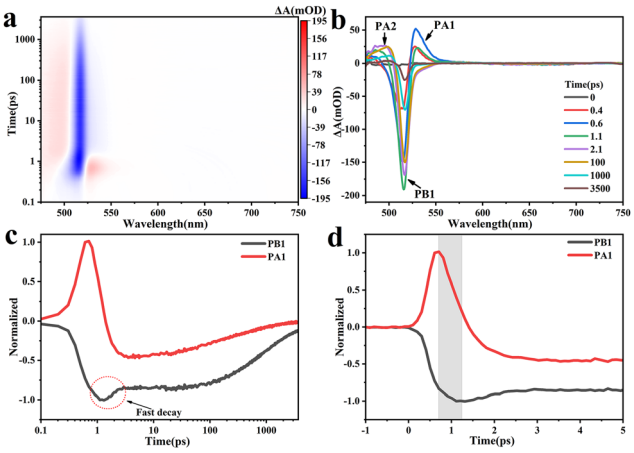

Fig. 2 (a) Two-dimensional pseudo colour diagram of TA spectra acquired at the internal region of the sample, (b) typical TA spectra at different delay times, (c) comparison of dynamic processes of PA1 and PB1 signals, and (d) dynamic processes of PA1 and PB1 signals within 5 picoseconds.

Published on 09 February 2023. Downloaded by Xian Jiaotong University on 12/4/2023 7:34:49 AM.

several typical spectra (Fig. 2(b)). We attribute the PB1 signal to the photo-induced bleaching of the ground state because the corresponding wavelength is close to the bandgap of the $CsPbBr_3$ perovskite ($\sim$2.4 eV),[36,37] while the PA1 signal is assigned to the hot carrier induced bandgap renormalization effect as this signal only exists for an extremely short time and is located at the red shift of the ground state bleaching signal.[38,39] As for signal PA2, it comes from the absorption of probe photons by electrons at the lowest energy level in the valence band after pump light excitation, thus locating at the nearest blue shift region of the ground state bleaching signal.[39]

In our experiments, the Gaussian distributed pump light could induce the nonuniform excitation in the irradiation area. As the TA signal was extracted from the probe light passing through the pump light irradiation region, the collected TA signal was the ensemble average of the whole interaction region in the sample. To avoid the density average effect caused by the nonuniform excitation of the pump light, only the probe light interacting with the central part of the pump light was collected. Pump fluence dependent TA spectra were also obtained to rule out the possible nonlinear effect caused by the intense pump light. Fig. S2 of the ESI† shows TA signals obtained at different light injection carrier concentrations, and the TA signal intensity as a function of the pump excitation is given in Fig. S3(a) and (c) (ESI†). The results indicate that the influence of the density average effect and nonlinear response in the experiments can be negligible.

Fig. 2(c) shows the temporal behaviour of the PA1 and PB1 signals. By comparison, we can find that there is an unusual phenomenon in the dynamics of PB1, as indicated by the red circle marker. At the beginning of the relaxation, there is a fast decay process, which shows a significantly different trend to the subsequent relaxation process. We speculate that this is caused by the decay of the hot carrier generated bleaching signal which is covered in the PB1 signal band. We can also see that due to the overlapping with the PB1 signal, the intensity of the PA1 signal finally decreases to a negative value. Fig. 2(d) rescales the time within 5 picoseconds to show more clearly how these two signals interact with each other. As indicated by the grey shaded region, the signal intensity of PA1 decreases while the intensity of PB1 increases, indicating the transition between both signals. Therefore, due to the mutual overlap of signal wavelength ranges, we can not obtain independent information, such as the energy state of carriers and their lifetimes. In order to separate these independent carrier physical processes and extract the corresponding information, it is necessary to conduct global fitting analysis[40,41] for the TA spectra.

By carrying out singular value decomposition (SVD) and creating a fitting model, we got the global fitting results as shown in Fig. 3(a) and (b). Fig. 3(a) shows the decay associated spectra (DAS), which provide information on the number of species and the corresponding characteristic TA spectra. Fig. 3(b) shows the change of species population relative to time, from which we can obtain the lifetime of each species and the mutual evolution process between them. In our results, three species are found as shown by the black line, the red line and the blue line, and their lifetimes are 522 fs, 304 ps and 1.94 ns, respectively. Considering the evolution between them, the three species can be attributed to hot carriers, carriers cooled to the bottom of the conduction band, and carriers trapped by defect states. The TA spectra of each species can be independently extracted by multiplying the data in Fig. 3(a) and (b) in matrix form. Fig. 3(c)–(e) represent the extracted TA spectra of hot carriers, cooled carriers, and trapped carriers, respectively. Furthermore, the overall TA spectra can be reproduced by summing them and the result is shown in Fig. 3(f). This reproduced result shows good agreement with the experimental data displayed in Fig. 2(a), indicating the high reliability of the global fitting.

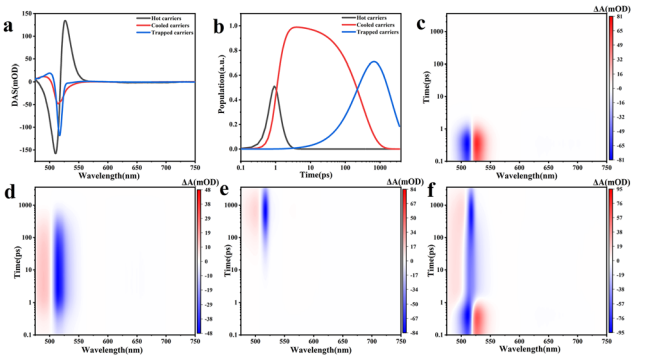

Fig. 3 Global fitting results of TA spectra acquired at the internal region of the sample, (a) decay associated spectra (DAS), (b) species population evolution *versus* time, TA spectra of hot carriers (c), cooled carriers (d) and trapped carriers (e) extracted from global fitting results, respectively, and (f) overall TA spectra reproduced from global fitting results.

Based on the global fitting results of TA spectra, the evolution of the photoinduced carriers can be deduced. As shown in Fig. 3(a) and (b), the first species (represented by the black line) produces a positive absorption signal and a negative absorption signal at the shorter wavelength region, and the signals last for about 3 ps. Considering that the photon energy of the 400 nm pump light is greater than the bandgap, the energy of the excited electrons is higher than the bottom of the conduction band, and their temperature is higher than the lattice. Electrons with this characteristic are usually called ''hot carriers''. The lifetime of hot carriers is extremely short, usually within hundreds of femtoseconds to a few picoseconds, which is consistent with 522 fs of our fitting results. To illustrate the energy state and dynamic process of carriers, a physical model[42,43] scheme is given in Fig. 4. Hot carriers are formed after the electrons in the valence band absorb the pump photon energy and transit to the conduction band (red-to-orange shaded region). Due to the occupation of high energy states and the bleaching of the valence band, this hinders the further absorption of photons with corresponding wavelengths in the probe light, inducing a negative absorption signal in the TA spectra. Meanwhile, at high excitation density, the screening effect caused by the exchange and correlation relationship between hot electron–hole pairs will reduce the energy of perovskite films and make the lowest energy level of the valence

 This journal is © The Royal Society of Chemistry 2023

Published on 09 February 2023. Downloaded by Xian Jiaotong University on 12/4/2023 7:34:49 AM.

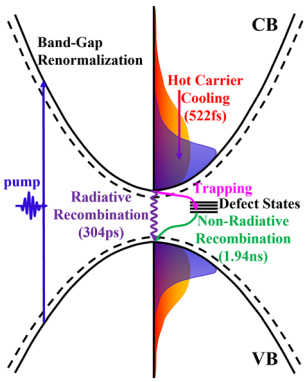

Fig. 4 Physical model of carrier transition and relaxation process at the internal region.

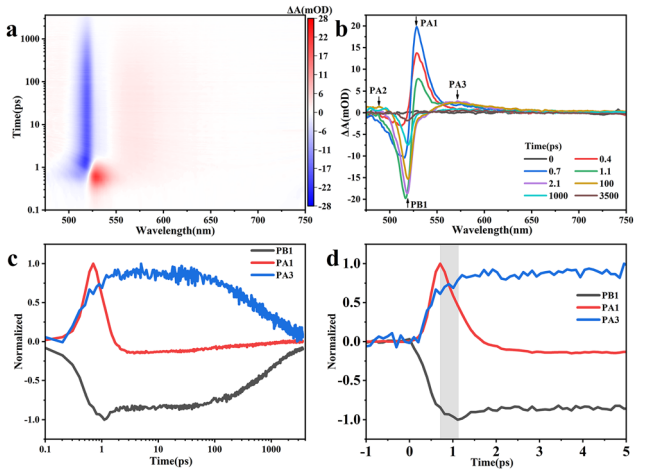

Fig. 5 (a) Two-dimensional pseudo colour diagram of TA spectra acquired at the boundary region of the sample, (b) typical TA spectra at different delay times, (c) comparison of dynamic processes of PA1, PB1 and PA3 signals, and (d) dynamic processes of PA1, PB1 and PA3 signals within 5 picoseconds.

band and conduction band shift. Besides, the nonuniform distribution of free carriers could introduce the band tail states, causing the disturbance of the valence and conduction band edge. These effects may lead to the renormalization of the bandgap and make the bandgap shrink (as indicated by the dashed parabolic line in Fig. 4), which has been theoretically and experimentally studied in semiconductors such as transition metal dichalcogenides, perovskites, and some traditional semiconductors.[42–46] The transition between the new band edges produced by bandgap renormalization leads to a positive absorption signal in the TA spectra.

After undergoing the relaxation process with a lifetime of 522 fs, hot carriers release extra energy to the lattice and gradually cool down to the bottom of the conduction band (blue shaded region). Corresponding to the second species in Fig. 3(b), the intensity of the black line decreases while the intensity of the red line increases. Therefore, the species represented by the red line is assigned to cooled carriers. This species will also produce a bleaching signal, which prohibits the transition from the top of the valence band to the bottom of the conduction band, that is, ground state bleaching. As discussed above, the ground state bleaching will be sandwiched between the negative absorption signal and the positive absorption signal caused by hot carriers. One part of the cooled carriers recombines with the holes in the valence band by radiating photons, with a lifetime of 304 ps, and the other part is transferred to the defect states and trapped. The species of the trapped carriers is represented by the blue line, which generates the bleaching signal because the valence band is still partially depopulated. It can be deduced from the kinetic curve that the trapped carriers gradually increase in the process of cooled carrier reduction, and then return to the ground state through the non-radiative recombination process with a lifetime of 1.94 ns. So far, the evolution and dynamics of photoinduced carriers including hot carriers, and recombination and transition of cooled carriers have been clarified by global fitting of the TA spectra in perovskite films. This forms the basis of carrier dynamics in the boundary region of the film as discussed below.

Under the same experimental conditions, we carried out a TAM test at the boundary region of single crystalline perovskite films to characterize the difference with the internal region. Multiple experiments were also conducted at different sites of the boundary region, and the results are shown in Fig. S4 of the ESI.† Fig. 5(a) shows the pseudo colour diagram of the TA signal acquired at the boundary region of single crystalline perovskite films. The evolution of several typical spectra at different delay times is shown in Fig. 5(b). We can see clearly that in addition to the basic characteristics of the TA spectra acquired at the internal region, there is an additional broadband positive absorption signal (PA3) ranging from 550 nm to 650 nm. As presented in Fig. S5 (ESI†), by comparing the normalized TA spectra of the boundary region with the internal region at the same time delay, it is obvious that the positive absorption signal at the boundary region is significantly stronger than that at the internal region, indicating that carriers undergo a more complex dynamic process at the boundary.

Pump fluence dependent TA spectra were also acquired at the boundary region and the results are shown in Fig. S6 (ESI†). The signal intensity is also linear to pump excitation as presented in Fig. S3(b) and (d) (ESI†). From the steady-state absorption spectra and the change of transmitted light intensity with the incident light intensity of the pump light as given in Fig. S7 and S8 (ESI†), we further confirm that the sample has a strong absorption at 400 nm, and maintains a linear absorption to the pump light within the range of the fluences used in the experiments.

In Fig. 5(c) and (d), we compared the dynamics of PA1, PB1 and PA3 signals. We can see that PB1 and PA3 share almost the same evolution process. This means that the carriers generating the PB1 signal also contribute to the PA3 signal. As discussed above, the PB1 signal band contains negative absorption signals generated by cooled carriers and trapped carriers. Considering that there are a large number of different kinds of complex defect states at the boundary, the PA3 signal may be partly from the transition of the cooled carriers to the defect states,

Published on 09 February 2023. Downloaded by Xian Jiaotong University on 12/4/2023 7:34:49 AM.

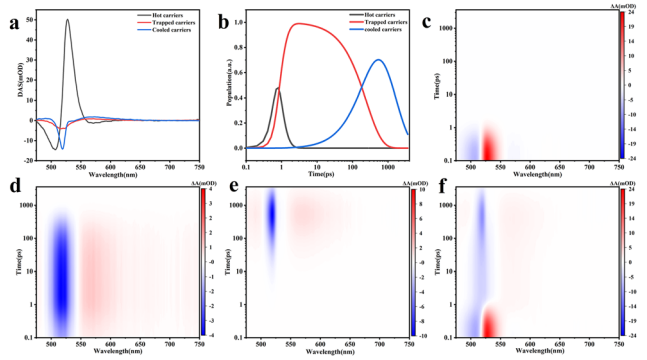

Fig. 6 Global fitting result of TA spectra acquired at the boundary region of the sample. (a) Decay associated spectra (DAS), (b) species population evolution *versus* time, TA spectra of hot carriers (c), cooled carriers (d) and trapped carriers (e) extracted from global fitting results, respectively, and (f) overall TA spectra reproduced from global fitting results.

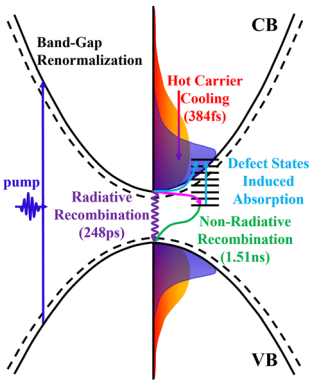

Fig. 7 Physical model of carrier transition and relaxation process at the boundary region.

and partly from the intra band absorption of carriers trapped by the defect states. Therefore, the energy levels of the defect states may cover a wide range, and the structure is very complex. This phenomenon has not been observed in the internal region, which may be due to the fewer defect states in the internal region.

Global fitting analysis was also carried out on this set of data as shown in Fig. 6. Fig. 6(a) and (b) show the DAS result and population evolution process. The time components are 384 fs, 248 ps, and 1.51 ns for hot carriers, cooled carriers and trapped carriers, respectively. These timescales are shorter compared to those acquired at the internal region, which may be attributed to the large density of defects at the boundary providing more additional channels for carrier relaxation and accelerating the recombination process. Fig. 6(c)–(f) show extracted TA spectra of each species and the overall spectra, which also show good agreement with the experimental data. From the extracted TA spectra of cooled carriers and trapped carriers displayed in Fig. 6(d) and (e), we can see that both kinds of carriers cause broadband absorption in the long wave direction, which is consistent with the results discussed above.

Based on the global fitting results of the boundary region data, we also proposed a suitable physical model to describe the carrier dynamics process at this region of single crystalline perovskites, as shown in Fig. 7. When the hot carriers have cooled to the bottom of the conduction band, some carriers are trapped by the defect states, and the others recombine with the holes in the form of radiation. The difference from the carrier dynamics at the internal region is that the carriers trapped by the defect states can also absorb the energy of the probe light forming an intra-band transition. By fs-TAM measurements and global fitting analysis in different areas of perovskite films, the influences of defects in the crystal on the carrier dynamics are clarified.

3. Experimental methods

Preparation of $CsPbBr_3$ perovskite single crystalline films

4.5 mmol caesium bromide (CsBr, 99.9%, Meryer) and 4.5 mmol lead bromide ($PbBr_2$, 99%, Meryer) were dissolved in 10 ml dimethyl sulfoxide (DMSO, 99.9%, Aladdin) in ambient air and stirred at 50 °C until the solution became transparent. The cooling precursor solution was titrated with 11 ml acetonitrile (MeCN, ≥99.9%, Aladdin) and then stirred for 24 h at 50 °C. After that, supernatant liquid was filtered with poly tetra fluoroethylene (PTFE) 0.2 μm pore-size syringe filters for crystal growth. 10 μl saturated solution was dropped between two clean quartz substrates. The two substrates with precursor solution were clamped to apply pressure uniformly and then were placed in a sealed container filled with 10 ml MeCN at 40 °C for 12 hours. With the slow diffusion of MeCN vapor into saturated precursor solution, $CsPbBr_3$ single crystalline films were achieved on quartz substrates.

Femtosecond transient absorption microscopy setup

The femtosecond laser light source we used was output by a Ti:Sapphire femtosecond laser amplifier (Coherent, Libra), with a central wavelength of 800 nm, a pulse width of 50 fs and a repetition frequency of 1 kHz. A beam splitter was used to divide the light source into two, one of which was used to excite a β-BBO crystal generating the second harmonic with a central wavelength of 400 nm. The other beam was focused into sapphire to generate white light supercontinuum (WLC) through self-phase modulation as the probe light. Then the pump light and probe light overlapped spatially through a dichroic mirror (Thorlabs, DMLP425), and were focused on the sample using a 20× objective lens (Olympus). The laser passing through the sample was collimated using a 10× objective lens (Nikon) and the pump light was filtered using a long-pass filter with a cut-off wavelength of 450 nm (Thorlabs, FEL0450). Considering the Gaussian distribution of the pump light, to avoid the density average effect induced by the nonuniform excitation, an aperture was placed after the sample and only the central part of the probe beam was collected using the collimating lens. The probe light was then received using a spectrometer (Avantes). By adjusting the delay time between the pump and probe pulses, TA spectra ranging from 475 to 750 nm were recorded. The time resolution of the probe light is characterized by optical Kerr gate technology, and the results are shown in the ESI,† Fig. S9.

 This journal is © The Royal Society of Chemistry 2023

Published on 09 February 2023. Downloaded by Xian Jiaotong University on 12/4/2023 7:34:49 AM.

4. Conclusions

In summary, we have studied the photoinduced carrier dynamics in $CsPbBr_3$ single crystalline perovskites in detail by using fs-TAM technology. By comparing the carrier dynamics between the boundary region with high defect density and the internal region with low defect density, we found that complex defect states at the boundary region will cause further absorption of carriers at the bottom of the conduction band and intraband absorption of defect state energy levels. The lifetimes of carriers will also be shortened. This work provides a direct demonstration of the influence of defects on the carrier dynamics in perovskite films, and can also provide some guiding suggestions for the fabrication of single crystalline perovskite devices. Taking some surface treatment of the material, reducing the density of defect states at the boundary of the materials may be useful to improve the device performance.

Conflicts of interest

There are no conflicts to declare.

Acknowledgements

This work was supported by the National R&D Program of China (Grant No. 2019YFA0706402) and the National Natural Science Foundation of China (Grant No. 62027822).

References

1 S. D. Stranks and H. J. Snaith, *Nat. Nanotechnol.*, 2015, **10**, 391–402.
2 J. S. Manser, J. A. Christians and P. V. Kamat, *Chem. Rev.*, 2016, **116**, 12956–13008.
3 J. Huang, Y. Yuan, Y. Shao and Y. Yan, *Nat. Rev. Mater.*, 2017, **2**, 1–19.
4 T. M. Brenner, D. A. Egger, L. Kronik, G. Hodes and D. Cahen, *Nat. Rev. Mater.*, 2016, **1**, 1–16.
5 S. D. Stranks, G. E. Eperon, G. Grancini, C. Menelaou, M. J. P. Alcocer, T. Leijtens, L. M. Herz, A. Petrozza and H. J. Snaith, *Science*, 2013, **342**, 341–344.
6 R. J. Sutton, G. E. Eperon, L. Miranda, E. S. Parrott, B. A. Kamino, J. B. Patel, M. T. Horantner, M. B. Johnston, A. A. Haghighirad, D. T. Moore and H. J. Snaith, *Adv. Energy Mater.*, 2016, **6**, 1502458.
7 G. E. Eperon, S. D. Stranks, C. Menelaou, M. B. Johnston, L. M. Herz and H. J. Snaith, *Energy Environ. Sci.*, 2014, **7**, 982–988.
8 D. Shi, V. Adinolfi, R. Comin, M. J. Yuan, E. Alarousu, A. Buin, Y. Chen, S. Hoogland, A. Rothenberger, K. Katsiev, Y. Losovyj, X. Zhang, P. A. Dowben, O. F. Mohammed, E. H. Sargent and O. M. Bakr, *Science*, 2015, **347**, 519–522.
9 Z. Chen, Q. Dong, Y. Liu, C. Bao, Y. Fang, Y. Lin, S. Tang, Q. Wang, X. Xiao, Y. Bai, Y. Deng and J. Huang, *Nat. Commun.*, 2017, **8**, 1–7.
10 Z. Chen, B. Turedi, A. Y. Alsalloum, C. Yang, X. Zheng, I. Gereige, A. AlSaggaf, O. F. Mohammed and O. M. Bakr, *ACS Energy Lett.*, 2019, **4**, 1258–1259.
11 A. Y. Alsalloum, B. Turedi, X. P. Zheng, S. Mitra, A. A. Zhumekenov, K. J. Lee, P. Maity, I. Gereige, A. AlSaggaf, I. S. Rogan, O. F. Mohammed and O. M. Bakr, *ACS Energy Lett.*, 2020, **5**, 657–662.
12 W. Zhang, L. Chen, Z. Zou, Z. Nan, J. Shi, Q. Luo, Y. Hui, K. Li, Y. Wang, J. Zhou, J. Yan and B. Mao, *ACS Appl. Mater. Interfaces*, 2022, **14**, 31911–31919.
13 E. Aydin, M. De Bastiani and S. De Wolf, *Adv. Mater.*, 2019, **31**, 1900428.
14 Z. Ni, H. Jiao, C. Fei, H. Gu, S. Xu, Z. Yu, G. Yang, Y. Deng, Q. Jiang, Y. Liu, Y. Yan and J. Huang, *Nat. Energy*, 2022, **7**, 65–73.
15 Y. Chen, L. Zhang, Y. Zhang, H. Gao and H. Yan, *RSC Adv.*, 2018, **8**, 10489–10508.
16 L. Cai, L. Liang, J. Wu, B. Ding, L. Gao and B. Fan, *J. Semicond.*, 2017, **38**, 014006.
17 P. K. Nayak, D. T. Moore, B. Wenger, S. Nayak, A. A. Haghighirad, A. Fineberg, N. K. Noel, O. G. Reid, G. Rumbles, P. Kukura, K. A. Vincent and H. J. Snaith, *Nat. Commun.*, 2016, **7**, 1–8.
18 T. A. S. Doherty, A. J. Winchester, S. Macpherson, D. N. Johnstone, V. Pareek, E. M. Tennyson, S. Kosar, F. U. Kosasih, M. Anaya, M. Abdi-Jalebi, Z. Andaji-Garmaroudi, E. L. Wong, J. Madeo, Y. H. Chiang, J. S. Park, Y. K. Jung, C. E. Petoukhoff, G. Divitini, M. K. L. Man, C. Ducati, A. Walsh, P. A. Midgley, K. M. Dani and S. D. Stranks, *Nature*, 2020, **580**, 360–366.
19 J. P. Correa-Baena, Y. Luo, T. M. Brenner, J. Snaider, S. Sun, X. Li, M. A. Jensen, N. T. P. Hartono, L. Nienhaus, S. Wieghold, J. R. Poindexter, S. Wang, Y. S. Meng, T. Wang, B. Lai, M. V. Holt, Z. Cai, M. G. Bawendi, L. Huang, T. Buonassisi and D. P. Fenning, *Science*, 2019, **363**, 627–631.
20 Y. Yang, M. Yang, D. T. Moore, Y. Yan, E. M. Miller, K. Zhu and M. C. Beard, *Nat. Energy*, 2017, **2**, 1–7.
21 Z. Ni, C. Bao, Y. Liu, Q. Jiang, W. Wu, S. Chen, X. Dai, B. Chen, B. Hartweg, Z. Yu, Z. Holman and J. Huang, *Science*, 2020, **367**, 1352–1358.
22 B. Turedi, V. Yeddu, X. Zheng, D. Y. Kim, O. M. Bakr and M. I. Saidaminov, *ACS Energy Lett.*, 2021, **6**, 631–642.
23 Y. Zhu, Q. Cui, J. Chen, F. Chen, Z. Shi, X. Zhao and C. Xu, *ACS Appl. Mater. Interfaces*, 2021, **13**, 6820–6829.
24 W. Liu, H. Yu, Y. Li, A. Hu, J. Wang, G. Lu, X. Li, H. Yang, L. Dai, S. Wang and Q. Gong, *Nano Lett.*, 2021, **21**, 2932–2938.
25 G. J. A. Wetzelaer, M. Scheepers, A. M. Sempere, C. Momblona, J. Ávila and H. J. Bolink, *Adv. Mater.*, 2015, **27**, 1837–1841.
26 S. D. Stranks, *ACS Energy Lett.*, 2017, **2**, 1515–1525.
27 C. M. Wolff, P. Caprioglio, M. Stolterfoht and D. Neher, *Adv. Mater.*, 2019, **31**, 1902762.
28 M. Lorenc, M. Ziolek, R. Naskrecki, J. Karolczak, J. Kubicki and A. Maciejewski, *Appl. Phys. B: Lasers Opt.*, 2002, **74**, 19–27.
29 R. Berera, R. van Grondelle and J. Kennis, *Photosynth. Res.*, 2009, **101**, 105–118.
30 Y. Sun, Y. Fang, Z. Li, J. Yang, X. Wu, J. Jia, K. Liu, L. Chen and Y. Song, *Front. Mater.*, 2021, **8**, 475.
31 M. C. Fischer, J. W. Wilson, F. E. Robles and W. S. Warren, *Rev. Sci. Instrum.*, 2016, **87**, 031101.

Published on 09 February 2023. Downloaded by Xian Jiaotong University on 12/4/2023 7:34:49 AM.

32 D. Y. Davydova, A. de la Cadena, D. Akimov and B. Dietzek, *Laser Photonics Rev.*, 2016, **10**, 62–81.
33 Y. Zhu and J. Cheng, *J. Chem. Phys.*, 2020, **152**, 020901.
34 S. Nah, B. Spokoyny, C. Stoumpos, C. M. M. Soe, M. Kanatzidis and E. Harel, *Nat. Photonics*, 2017, **11**, 285–288.
35 Z. Yang, Q. Xu, X. Wang, J. Lu, H. Wang, F. Li, L. Zhang, G. Hu and C. Pan, *Adv. Mater.*, 2018, **30**, 1802110.
36 E. L. Unger, L. Kegelmann, K. Suchan, D. Sörell, L. Korte and S. Albrecht, *J. Mater. Chem. A*, 2017, **5**, 11401–11409.
37 X. Wang, J. He, J. Li, G. Lu, F. Dong, T. Majima and M. Zhu, *Appl. Catal., B*, 2020, **277**, 119230.
38 Z. Guo, Y. Wan, M. Yang, J. Snaider, K. Zhu and L. Huang, *Science*, 2017, **356**, 59–62.
39 N. Mondal and A. Samanta, *Nanoscale*, 2017, **9**, 1878–1885.
40 C. Ruckebusch, M. Sliwa, P. D. Pernot, A. De Juan and R. Tauler, *J. Photochem. Photobiol., C*, 2012, **13**, 1–27.
41 J. J. Snellenburg, S. Laptenok, R. Seger, K. M. Mullen and I. H. van Stokkum, *J. Stat. Softw.*, 2012, **49**, 1–22.
42 J. Y. Sung, C. Schnedermann, L. Ni, A. Sadhanala, R. Chen, C. Cho, L. Priest, J. M. Lim, H. K. Kim, B. Monserrat, P. Kukura and A. H. Rao, *Nat. Phys.*, 2020, **16**, 171–176.
43 M. B. Price, J. Butkus, T. C. Jellicoe, A. Sadhanala, A. Briane, J. E. Halpert, K. Broch, J. M. Hodgkiss, R. H. Friend and F. Deschler, *Nat. Commun.*, 2015, **6**, 1–8.
44 G. Trankle, E. Lach, A. Forchel, F. Scholz, C. Ell, H. Haug, G. Weimann, G. Griffiths, H. Kroemer and S. Subbanna, *Phys. Rev. B: Condens. Matter Mater. Phys.*, 1987, **36**, 6712.
45 D. Auvergne, J. Camassel and H. Mathieu, *Phys. Rev. B: Condens. Matter Mater. Phys.*, 1975, **11**, 2251–2259.
46 M. M. Ugeda, A. J. Bradley, S. F. Shi, F. H. da Jornada, Y. Zhang, D. Y. Qiu, W. Ruan, S. K. Mo, Z. Hussain, Z. X. Shen, F. Wang, S. G. Louie and M. F. Crommie, *Nat. Mater.*, 2014, **13**, 1091–1095.

 This journal is © The Royal Society of Chemistry 2023